ACS NANO
Cite This: ACS Nano 2018, 12, 12692−12700
www.acsnano.org

ARTICLE

Prismatic Deflection of Live Tumor Cells and Cell Clusters

Peter M. Aldridge,[†,⊥] Monorina Mukhopadhyay,[‡,⊥] Sharif U. Ahmed,[§] Wendi Zhou,[‡] Elisa Christinck,[§] Rhema Makonnen,[§] Edward H. Sargent,[‡] and Shana O. Kelley*[,†,§]

[†]Institute for Biomaterials and Biomedical Engineering, [‡]Department of Electrical & Computer Engineering, and [§]Department of Pharmaceutical Sciences, University of Toronto, Toronto, ON M5S3M2, Canada

Supporting Information

ABSTRACT: The analysis of heterogeneous subpopulations of circulating tumor cells (CTCs) is critical to enhance our understanding of cancer metastasis and enable noninvasive cancer diagnosis and monitoring. The phenotypic variability and plasticity of these cells—properties closely linked to their clinical behavior—demand techniques that isolate viable, discrete fractions of tumor cells for functional assays of their behavior and detailed analysis of biochemical properties. Here, we introduce the Prism Chip, a high-resolution immunomagnetic profiling and separation chip which harnesses a cobalt-based alloy to separate a flowing stream of nanoparticle-bound tumor cells with differential magnetic loading into 10 discrete streams. Using this approach, we achieve exceptional purity (5.7 log white blood cell depletion) of isolated cells. We test the differential profiling function of the integrated device using prostate cancer blood samples from a mouse xenograft model. Using integrated graphene Hall sensors, we demonstrate concurrent automated profiling of single cells and CTC clusters that belong to distinct subpopulations based on protein surface expression.

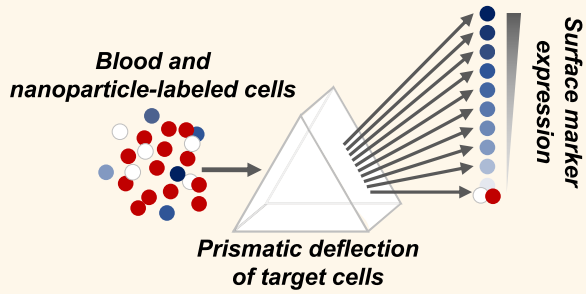

KEYWORDS: *circulating tumor cell, cell analysis, prismatic deflection, phenotypic profiling, Hall sensor, CTC cluster*

Identifying circulating tumor cells (CTCs) that possess high metastatic potential is a pressing problem in cancer research.[1] Cancer metastasis is the step that converts local, confined disease to a deadly condition affecting distal sites, and CTCs are the initiators of metastatic disease.[2] However, not all blood-borne tumor cells are able to colonize metastatic tumors. It is therefore critical that specific subpopulations of cells are identified and isolated to enable further insight into the biology of metastasis, the treatment of metastatic disease, and the development of effective liquid biopsy approaches for cancer diagnosis and management.[1−3]

There exists a correlation between the number and type of CTCs in the bloodstream and the progression of cancer.[4,5] Unfortunately, the enumeration of CTCs has, to date, not proven clinically actionable. There is growing recognition that CTCs are highly heterogeneous, and that characterizing phenotypic subpopulations of these cells, rather than simply establishing levels of blood-borne cells, will be needed to provide the data required for clinical action.

CTCs become phenotypically heterogeneous through processes such as the epithelial−mesenchymal transition (EMT), whereby cell−cell adherence proteins are lost, and cells take on more mesenchymal properties. This phenotypic shift enhances the ability of CTCs to survive in circulation and colonize distal sites.[6] In addition, clusters of CTCs are an important subpopulation of cells. It has recently been shown that the relative level of single cells *versus* cell clusters in a patient sample can provide insight into the aggressiveness of a patient's cancer and offers prognostic value.[7] Immunoaffinity assays have been developed to purify CTCs from the immense background of whole blood; however, most existing technologies do not resolve subpopulations, nor do they resolve single CTCs *versus* clusters without end point staining.[1]

Measuring the level of proteins found on a cell's surface provides a means to distinguish among phenotypic subpopulations of CTCs.[8,9] The most common method for measuring cell surface protein levels—fluorescence-activated cell sorting (FACS)—does not succeed in high-background biological samples such as whole blood; instead, it requires extensive sample purification prior to analysis.[10] Immunomagnetic separation has been used to isolate or capture magnetically labeled cancer cells. However, most present-day techniques lack the resolution necessary to quantitatively profile surface protein expression of rare cells and instead only offer a binary assay that indicates the presence or absence of a given protein.[11,12]

Received: October 6, 2018
Accepted: November 16, 2018
Published: November 16, 2018

Downloaded via UNIV OF TORONTO on January 14, 2019 at 17:16:20 (UTC).
See https://pubs.acs.org/sharingguidelines for options on how to legitimately share published articles.

© 2018 American Chemical Society

DOI: 10.1021/acsnano.8b07616
ACS Nano 2018, 12, 12692−12700

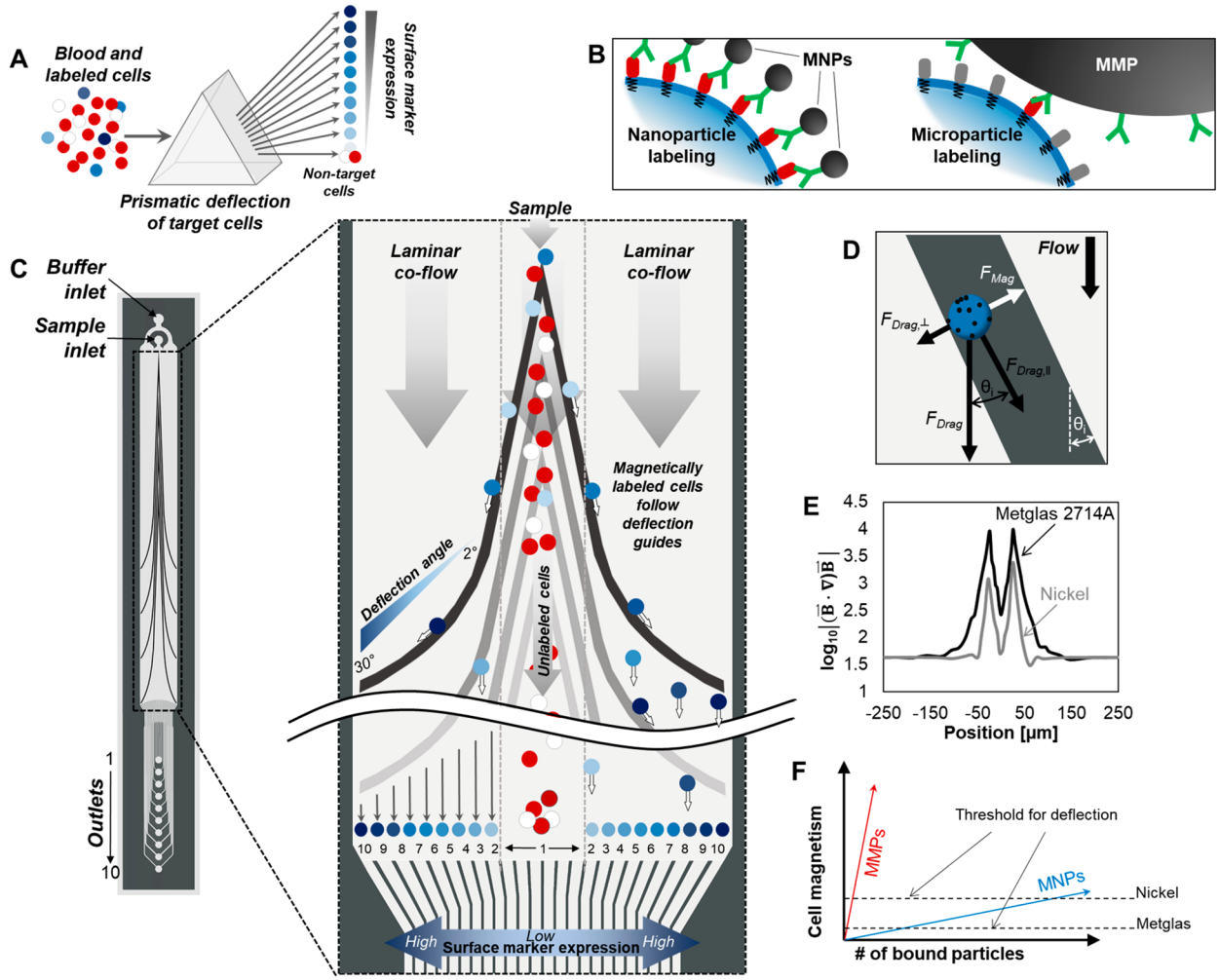

Figure 1. Design of the Prism Chip. (A) Prismatic deflection separates a continuous sample stream into discrete subpopulations based on surface marker expression. (B) Magnetic nanoparticles offer a more faithful representation of cell surface protein expression than larger magnetic microparticles. (C) Schematic of the Co-based ribbon prismatic deflection chip (not drawn to scale). Deflection guides are made up of distinct segments having angles ranging from 2 to 30°. (D) Forces acting on a cell in the horizontal plane (neglecting friction). Magnetically labeled cells will follow the deflection guides until the magnetic force pulling the cells toward the guide is overcome by the component of the drag force acting perpendicular to the guide. (E) Comparison of the magnetic field enhancement generated with nickel and Co-based deflection guides using COMSOL Multiphysics. (F) Qualitative comparison of factors that affect cell deflection. Co-based deflection requires less particle loading for efficient deflection than comparable nickel-based guides.

Advanced immunomagnetic devices have been reported that use an external magnetic field to deflect micro- or nanoparticle-laden cells from a flowing liquid stream. These have included systems coupled with integrated ferromagnetic elements that achieve a level of focused control over the applied magnetic field.[13,14] Immunomagnetic techniques have been adapted to separate distinct cellular subpopulations, either by exploiting differences in particle labeling efficiency or by using differently sized magnetic particles targeted to nonoverlapping populations.[15,16] In our laboratories, we developed a technique referred to as magnetic ranking cytometry that separates and profiles rare cancer cells according to levels of surface protein expression or intracellular mRNAs.[17,18] This method achieves a high level of sensitivity and finely resolves cancer cells exhibiting subtle changes in phenotype but does not allow the retrieval of live cells or cell clusters. Thus, there exists a need for an approach that can isolate cell subpopulations with high resolution, distinguish between single cells and cell clusters, and do so in a nondestructive manner that preserves cell viability for ensuing downstream assays.

Here, we present a microfluidic device that isolates magnetically-labeled cells and separates them into distinct subpopulations corresponding to their surface protein expression levels. We achieve this using variably angled ferromagnetic guides (Figure 1) and the concept of prismatic deflection: the approach separates a flowing stream of cells into discrete fractions, analogous to the functioning of an optical prism dispersing light into its component wavelengths (Figure 1A).

We enumerate thereby the subpopulations of cells, interrogating outlet channels using integrated graphene Hall sensors, and collect the sorted cells under continuous flow for further downstream analysis and culture. The integrated devices combine concurrent profiling of CTCs and CTC clusters in a nondestructive manner. The design reliably and accurately profiles the surface expression of a range of cancer cell lines in both buffer and blood and achieves a 5.7 log depletion of white blood cells when sorting biological samples.

DOI: 10.1021/acsnano.8b07616
ACS Nano 2018, 12, 12692−12700

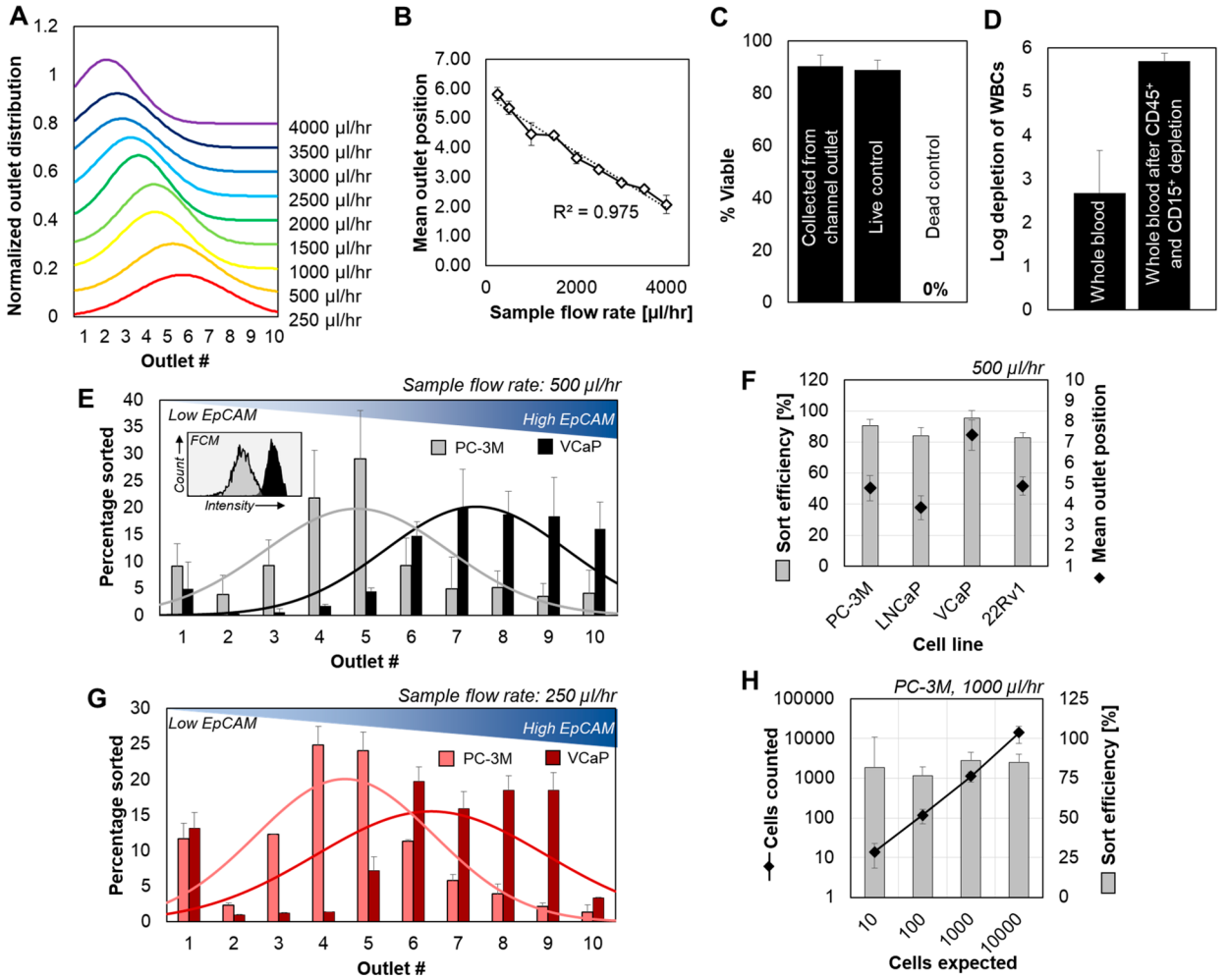

Figure 2. Performance of the Prism Chip. (A,B) Changing the flow rate (drag force) alters outlet position for sorted beads used as a model of cells. A linear relationship between drag force and outlet position was expected based on the range and gapping of the deflection angles. (C) Assessing viability of PC-3M cells after sorting. Live control was not sorted and kept on ice during the experiment; dead control was treated with 70% methanol. (D) WBCs are only deflected in the chip if they nonspecifically bind to the magnetic nanobeads, which is exceedingly rare. A negative depletion step prior to sorting leads to increased purity. (E) Profiling the EpCAM expression of PC-3M and VCaP cells suspended in aqueous buffer. Inset presents the EpCAM expression of PC-3M and VCaP as measured with flow cytometry. (F) Sort efficiency and mean outlet position of a variety of prostate cancer cell lines sorted in the Prism Chip. (G) The Prism Chip is capable of profiling surface marker expression of target cells suspended in blood, though at a lower throughput than in buffer. (H) The Prism Chip efficiently sorts both high and low concentrations of target cells.

RESULTS AND DISCUSSION

Overview of the Prism Chip. To separate and profile magnetically-labeled cells from whole blood samples, we designed a microfluidic chip that uses angled ferromagnetic guides in the presence of an external magnetic field to induce a lateral deflection of a magnetically-labeled target.[13,16,19] A wide range of differently sized beads are available and can be used to achieve magnetic labeling of a cellular target; however, to carry out not just separation, but profiling of cell surface protein expression, it is essential that the number of magnetic beads bound to the cell vary in direct proportion with protein expression. Large magnetic microparticles (MMPs, with diameters on the order of 1−5 μm) can occlude antibody binding sites, whereas magnetic nanoparticles (MNPs) having diameters below 100 nm avoid this problem (Figure 1B).

One added challenge, though, is that MNPs provide a smaller total magnetized volume and thus a reduced magnetic force for a given applied field. To achieve high sorting efficiency and throughput while using MNPs for labeling, we harnessed the high magnetic permeability of a cobalt-based magnetic alloy (μ/μ_o = 80 000) to enhance the external magnetic field.[20]

Fabrication of the Prism Chip is outlined in the Supporting Information (SI Figure S1). Briefly, sheets of the Co-alloy are attached to a glass wafer and are then patterned *via* wet-etching into deflection guides made up of 10 discrete segments with increasingly steep angles relative to the direction of flow. Fluidic channels are then patterned overtop of the ferromagnetic ribbons, and the whole assembly is capped with polydimethylsiloxane (PDMS) containing inlet and outlet ports. A syringe pump drives flow to two separate chip inlets, one for cell samples and one for a flow-focusing buffer stream. A neodymium magnet is placed underneath the fluidic channel to generate an external magnetic field, and the ferromagnetic guides generate local field enhancements. Magnetically labeled cells flowing in the focused central stream are deflected by the combination of magnetic capture forces (localized to the edges of the ferromagnetic guides) and fluidic drag forces, whereas

DOI: 10.1021/acsnano.8b07616
ACS Nano 2018, 12, 12692−12700

nontarget cells do not experience any magnetic force and are directed to a waste outlet by drag force alone (Figure 1C). The magnitude of the magnetic capture force is dictated by the amount of magnetic loading on the surface of the cell, while the direction of the magnetic force is dictated by the angle of the deflection guides relative to the direction of flow. Deflection angles were patterned at angles ranging from 2 to 30°, in a progression which yielded a linear increase in the sine of the deflection angle (SI Figure S3). Each cell reaches its maximal deflection when the magnetic trapping force is too small to balance the component of the fluidic drag force acting perpendicular to the ferromagnetic guides (Figure 1D). Deflected cells that fall off of the guides flow straight to the end of the microfluidic channel, where they are directed to one of 10 outlets. These outlets are then connected in series to channels with patterned graphene Hall sensors laid out under them, which are then used to classify the cells in each outlet bin as either single cell or multicellular cluster.

In simulations, the cobalt-based guides were shown to generate a field enhancement 6.5× larger than that produced by nickel alone and amplified the magnitude of external magnetic trapping force by over 3 orders of magnitude (Figure 1E; additional simulation details are available in SI Figure S4). We then validated the simulation results by comparing the performance of two sets of chips made with either nickel- or cobalt-based guides (SI Figure S5). A qualitative model presents the relative impact of using different magnetic beads and ferromagnetic guides on potential device performance (Figure 1F).

Performance of the Prism Chip. In the absence of a reliable method to generate targets having preciscely defined magnetic loading, we used variations in flow rate (and thus drag force) to characterize the linearity and reproducibility of the sorting and profiling method, with 8 μm magnetic microbeads serving as a cell analogue. Due to the high magnetic susceptibility of the microbeads, we carried out experiments with the beads suspended in a 75% glycerol solution to increase the drag force, allowing for lower flow rates and improved counting accuracy. The sample flow rate was varied from 250 to 4000 μL/h, generating a 16× range in drag force, which matched the approximate range in cell magnetism predicted to be the device operating range based on the design deflection angles (SI Figure S3). The distribution of beads at the outlet after sorting and the mean outlet position are plotted in Figure 2A,B, respectively. The mean outlet position showed a strong linear dependence on flow rate, indicating that the outlet position was proportional to the drag force acting on the beads, as intended in the chip design. This linearity allows for simple comparison of the magnetic loading between subpopulations profiled in different outlets.

We evaluated chip performance when profiling biological targets by sorting cultured prostate cancer cells. To evaluate the downstream viability of the cells after sorting, we labeled PC-3M cells with magnetic nanobeads, sorted them in the device, collected them at the outlet, and then assessed their viability using a commercial fluorescence kit. Cells were compared with an unsorted (live) and a methanol-treated (dead) control. Evaluation of cell viability after sorting showed no significant loss of viability when compared to unsorted cells (91 ± 4 and 89 ± 4% live cells, respectively) (Figure 2C; sample staining images are available in SI Figure S7). To quantify the prevalence of contaminating white blood cells (WBCs) while handling whole blood, we incubated whole blood samples with magnetic nanobeads targeted to EpCAM, sorted them through the chip, and every WBC which deviated from the waste outlet was deemed to be a contaminating cell when assessing log depletion of WBCs (Figure 2D).

To assess the ability of the Prism Chip to generate unique profiles in response to differences in magnetic loading, we sorted VCaP and PC-3M cells, separately, in buffer. Sorting was carried out using magnetic nanobeads targeted to EpCAM; VCaP is known to express high levels of EpCAM, whereas PC-3M's EpCAM expression ranges from low to moderately high.[21] Cells were stained with Syto 24 green, a fluorescent stain which exhibits a very strong fluorescent signal in the presence of nucleic acids, and were counted optically using fluorescence microscopy. Following sorting, the two cell lines exhibited the expected profiles, with VCaP cells being biased toward the high expression outlets (Figure 2E). We then performed a matched set of experiments using the same cell lines spiked into blood to demonstrate the efficacy of this system in working with biologically relevant samples (Figure 2G). The profiles generated in blood and in buffer were consistent with one another, though throughput was reduced when working with blood owing to its higher viscosity. When working with blood, the viscosity of the focusing buffer stream was increased by the addition of biocompatible sodium alginate (8 mg/mL) (SI Figure S8). Matching the viscosity of the sample and buffer streams was necessary to maintain their respective (design) widths in the chip.

The sorting efficiency (defined as the percentage of target cells directed away from the waste outlet) of the Prism Chip varies as a function of flow rate, cellular expression of the target surface marker, and the viscosity of the suspending medium. Figure 2F presents the sort efficiency of the device when sorting four different EpCAM expressing prostate cancer cell lines (PC-3M, LNCaP, VCaP, and 22Rv1), suspended in aqueous buffer, at a sample flow rate of 500 μL/h. An average sort efficiency of 88 ± 6% was achieved across these experiments, comparable to that of other microfluidic approaches. To evaluate the sensitivity of the chip, we prepared serial dilutions containing 10 000, 1000, 100, and 10 PC-3M cells/mL and sorted them. Sort efficiency was consistent across the samples, and the detected cell counts matched expectations (Figure 2H). A companion experiment, carried out in blood, is presented in the Supporting Information (SI Figure S9).

Integration of Hall Sensor Detectors. The Hall effect is the conversion of a magnetic field to a voltage difference across an electrical conductor or an electronic semiconductor, in the presence of a transverse applied electrical current. A Hall sensor is a four-terminal device that harnesses the Hall effect to convert changing magnetic fields into changing potential differences, or *vice versa*, using a semiconductor, and can therefore be used as a proximity sensor. The voltage response of a Hall sensor is characterized by the Hall coefficient (R_H), calculated as $V_H = R_H \frac{IB}{t}$, where V_H is the measured voltage and I and B are the current and magnetic intensity applied perpendicular to each other. The Hall coefficient depends on the mobility and charge carrier concentration of the sensor material.[22] As a result, semiconductor materials usually make effective Hall sensors, and graphene—a single-layer version of graphite—has a high Hall coefficient.[23] The Hall coefficient and the atomic thickness of monolayer graphene ensure that small changes in the magnetic field produce significant voltage

DOI: 10.1021/acsnano.8b07616
ACS Nano 2018, 12, 12692−12700

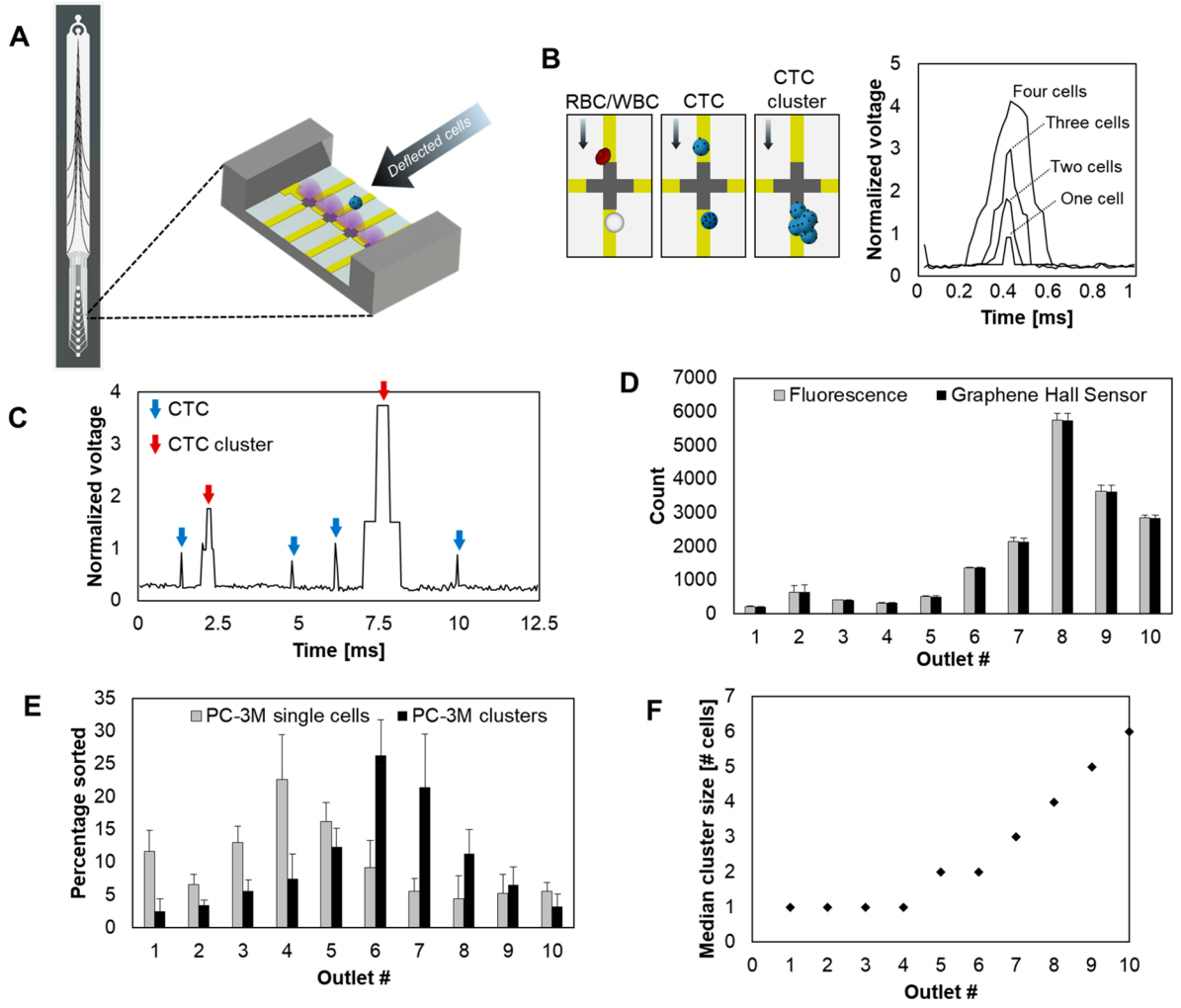

Figure 3. Differential classification of cells. (A) Sorted cells are enumerated by a collection of graphene Hall sensors. (B) Cells are classified into single cells or clusters by the magnitude of the sensor voltage response. (C) Voltage response of the sensor varies depending on the combination of size and magnetism of the cell or cell cluster. (D) Verification of device performance by comparing VCaP cell counts measured optically using fluorescence microscopy and counts determined from magnetic Hall sensor signals. (E) Hall sensor counts of both PC-3M single cells and artificial clusters spiked in blood. (F) Variation of mean cluster size *vs* the prismatic deflection chip bin, as measured by the Hall sensors.

responses. The sensitivity and specificity of a graphene Hall sensor, in addition to its high linear dynamic range and biocompatibility, make it an appealing material for cellular detection.[24]

Graphene sensors were patterned into a Greek-cross-shaped structure, which is established as the classical structure for effective Hall sensors with the lowest offset voltage. The sensing area of the sensors is the central area between the arms of the cross shape.[25] The sensors were laid out in a horizontal array across each channel to eliminate the need for flow-focusing structures, and flow channels were fabricated over the sensors. Each sensor recorded magnetic signals in the region vertically above it, and the sensors were used in combination to monitor the entire cross section of each outlet channel (Figure 3A). The devices had a minimum measured signal-to-noise ratio of 36.12 dB and a current sensitivity of 465.49 V/AT.

Differential Classification of Cells. Magnetically labeled cells flowing over the sensors induce a change in magnetism, depending on the cell's magnetic loading, which is proportional to its level of surface protein expression and its size. Larger cells and cell clusters have greater surface area, and, therefore, more surface biomarkers conjugated to magnetic particles on average, and produce voltage responses that are higher in magnitude and longer in duration (Figure 3B). Heterogeneous cells can therefore be differentiated by a Hall sensor due to their distinct magnetic signatures, by measuring the area under the curve (AUC) for the response peaks. The signals from the Hall sensor acquired and processed on an embedded processor provide the final counts of the cells obtained from the array of Hall sensors monitoring the profiled cells. Threshold values for the AUC were determined using theoretical models which were then refined using experimental data with the developed sensors.[25−27] The high linear range of the Hall sensors ensures that they do not saturate at high voltages, and this, along with the high signal-to-noise ratio of the devices, allows for small signal changes to be isolated in the presence of a strong magnetizing field.[23] Our method of electronic differential detection of a cellular cluster and single cells does not require the monitoring and processing equipment needed for fluorescence microscopy; this is an advantage when devising low-footprint solutions for disease detection.

DOI: 10.1021/acsnano.8b07616
ACS Nano 2018, 12, 12692−12700

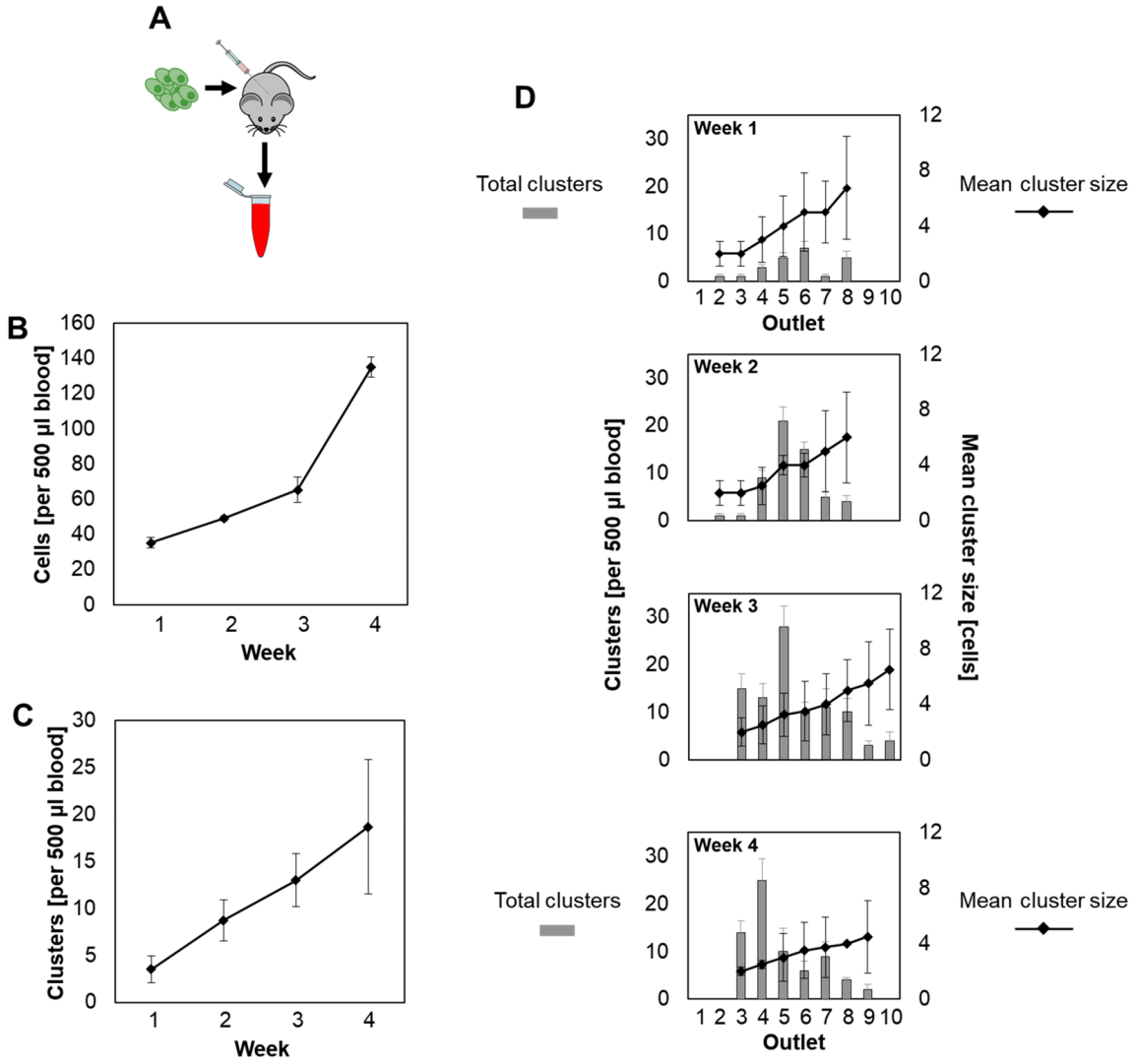

Figure 4. Profiling CTCs and CTC clusters in a mouse xenograft model. (A) Mouse xenograft models are generated by injecting prostate cancer cells in mice. (B) Count of the single cells obtained from 500 μL of mice blood over a 4 week period. (C) Count of clusters obtained per week from 500 μL of mouse blood. (D) Count and size of clusters detected in mice over 4 weeks, broken down by the Prism Chip outlet position. Data in (B–D) represent the average of five mice for the first 3 weeks and three mice for the fourth week.

Detection of Single CTCs and Clusters. We validated the magnetic sensing approach using magnetic microbeads of varying sizes. We used a mixture of beads of 10, 30, and 50 μm radius to characterize the ability of the Hall sensor to detect particles in flow over the sensor array. The percentage of each type of microbead detected by the sensor was within 2% of the input ratios in the solution (SI Figure S11).

We challenged the sensors using artificially created clusters of PC-3M cells to test the ability of the Hall sensors to distinguish between profiled single cells and clusters. PC-3M cells were artificially clustered and then incubated with anti-EpCAM beads and suspended in a buffer solution. The signals received from the Hall sensor for clusters of cells of various sizes are seen distinctly (Figure 3C).

We then conducted a set of experiments with the sensors integrated into the Prism Chip platform. We used three prostate cancer cell lines (VCaP, PC-3M, and PC-3) with known levels of EpCAM. The cells were incubated with anti-EpCAM beads in a buffered solution, profiled using the Prism Chip, and then enumerated using the integrated Hall sensors (SI Figure S13). The experiment for each cell line was repeated four times; in the first instance of these experiments, we also visually monitored each outlet of the deflection device for cell fluorescent signatures upstream of the Hall sensors and then correlated the results using the two enumeration methods. The counts from each method were found to agree with each other with >99% accuracy. Sample counts with VCaP cells are presented in Figure 3D. This confirms the robustness of the Hall sensor and the integration method.

The performance of the integrated devices was tested using a solution of both PC-3M single cells and cell clusters, spiked into whole blood. Cells and cell clusters were profiled in the deflection device and then separately enumerated using the Hall sensors (Figure 3E). As cell clusters are larger and have more exposed surface than single cells, they experience different forces in the deflection device. Assuming a roughly spherical cluster with comparable surface protein density of a single cell, the cluster with diameter D will experience a higher drag force ($F_D \propto D$) and higher magnetic force ($F_M \propto D^2$), resulting in a shift toward the outer outlets of the device (outlets 6–10). The median cluster size in each zone of the deflection device was obtained from these experiments (Figure

DOI: 10.1021/acsnano.8b07616
ACS Nano 2018, 12, 12692–12700

3F). The average cluster size of the artificial clusters was in the range of 2−3 single cells, and these were profiled in zones 6 and 7 of the deflection device. In preliminary experiments, the size of the clusters measured by the Hall sensors was confirmed by bright-field microscopy; a comparison of the counts with each method is presented in SI Figure S12.

Profiling of CTCs and Detection of Clusters in an Animal Model. We analyzed blood from mice bearing xenografted human prostate cancer tumors. PC-3M cells were injected orthotopically into the right dorsolateral lobe of the prostate of 6−8 week old male athymic nude (nu/nu) mice, and tumor progression was tracked in the mice over a month. We used a cohort of 20 mice, with blood obtained from five mice for weeks 1−3, and three mice for the final time point. The blood from the mice was depleted to remove white blood cells and then evaluated for EpCAM expression in both single cells and cell clusters using the integrated devices. The profile of the single cell and clusters of CTCs over a period of 4 weeks was measured per 500 μL of blood (Figure 4B,C). The epithelial marker expression decreased from week 1 to week 2, showing that the CTCs become more mesenchymal with tumor progression in this period. In weeks 3 and 4, the single-cell CTCs separate into two populations, one of low EpCAM mesenchymal cells and one of more epithelial cells (SI Figure S14). This is in keeping with previous experiments on CTCs.[28] In addition, the CTC levels rose as the tumors progressed in the xenografted mice.

The number of CTC clusters also increased with time. The median cluster size of CTCs was 2−4 cells, with the exception of week 1. In the first week, there were very few clusters (<5 in each blood sample); however, the average size of each cluster was larger (Figure 4D). A cluster of a particular size had an EpCAM expression lower than that of the corresponding artificial cluster, and this is due to the fact that artificial clusters are single cells that clump together, and their epithelial marker expression level is a factor of their size. A natural cluster found in a mouse blood sample contains an epithelial expression lower than that of an artificial cluster because clusters are more mesenchymal than single cells and indicate advanced stages of the disease.

CONCLUSIONS

The Prism Chip with integrated Hall sensors profiles both single cells and CTC clusters simultaneously and tracks the relative presence of single and multicellular CTCs in a disease model. This method of differential profiling of CTCs in blood provides a broader set of data for monitoring cancer progression and is a technique with interesting applications in CTC detection. Blood collected from mice with xenografted tumors was analyzed for CTCs, and the quantitative presence of CTC single cells and clusters and their related epithelial profiles were generated over the tumor progression.

This approach to differential profiling of CTCs does not capture the cells nor trap them. We showed that cells are undamaged and are available for further downstream processing and assays. The sensitive graphene Hall sensors eliminate the need for bulky microscopy and need neither human classification nor predictive algorithms for classification of the CTCs; instead, they generate electronic signals that are readily read using a simple embedded system. The profiling and enumeration devices are modular, and additional profiling levels or assays can be introduced between the two devices for further two- or three-dimensional profiling of the CTCs.

METHODS

Prism Chip Fabrication. Strips of Metglas 2714A were epoxy-bonded (Loctite M-31CL) onto 100 mm soda lime glass wafers (550 μm thick) and left to cure for 24 h. Excess epoxy was removed with acetone. The metallic surface was then primed with MCC 80/20 prior to spin-coating with a S1811 positive photoresist. The positive resist was photolithographically patterned, and then the exposed Metglas 2714A was etched using a mixture of 3.6% HCl, 14.3% H_2O_2, and 82.1% H_2O. After the remaining photoresist was stripped and the surface primed with OmniCoat to improve adhesion, the ferromagnetic guides were encapsulated with a layer of SU-8 3010, and then microfluidic channel features were patterned with a 50 μm layer of SU-8 3050. Each chip was then capped with cured PDMS with holes cored for all inlet and outlet ports, following an APTES treatment[29] (SI Figure S1).

Graphene Chip Fabrication. CVD films of monolayer graphene on silicon wafers (Graphenea) were patterned using electron beam lithography (EBL). Titanium (10 nm) and gold (50 nm) contacts were deposited using electron beam evaporation and patterned using EBL and a lift-off process, and the graphene crosses were defined using EBL with oxygen plasma etching. A 2 μm layer of SU-8 2002 (MicroChem) was used to protect the graphene sensors. The microfluidic channels were built using a 50 μm layer of SU-8 3050 with wet lithography. The devices were covered with APTES-treated cured PDMS (Dow Corning)[29] (SI Figure S2).

COMSOL Multiphysics Simulations. Measurements of the magnetic field enhancement generated by nickel and Metglas 2714A deflection guides were carried out in COMSOL Mutliphysics. Details of the simulation geometry and measurements are available in the Supporting Information (SI Figure S4).

Cancer Cell Lines. PC-3, PC-3M, and LNCaP human prostate cancer cells were acquired as a gift from Dr. Alison Allan's research group at London Health Sciences, London, ON, Canada. PC-3 cells were cultured in F12-K media, and the PC-3M and LNCaP cells were cultured in RPMI-1640 media. VCaP and 22Rv1 cells were acquired from ATCC. VCaP cells were cultured in DMEM, and 22Rv1 cells were cultured in RPMI-1640 media. All media were supplemented with 10% FBS and 1% penicillin−streptomycin. Cells were cultured at 37 °C and 5% CO_2.

Preparation of Cells for Deflection Experiments. Cells were harvested from culture flasks using a solution of 0.25% Trypsin and 1 mM ethylenediaminetetraacetic acid (EDTA) for approximately 5 min. After the cells had detached from the culture flask, the trypsin was immediately neutralized with buffer solution containing at least 10% FBS. Cells were then washed in a centrifuge at 200g for 5 min and then resuspended at an appropriate concentration in solution of Hanks' balanced salt solution (HBSS) supplemented with 2% BSA and 5 mM EDTA. Cells were magnetically labeled with CD326 (EpCAM) microbeads (130-061-101, MACS-dextran ferrite colloids beads with a diameter of 50 nm, purchased from Miltenyi Biotec); beads were added to all cell suspensions at a 20% concentration by volume. For experiments requiring optical profiling of the cells, Syto 24 green fluorescent nucleic acid stain (S7559, ThermoFisher) was added to the cell suspension at a concentration of ≥1 μL/mL. Artificial clusters were generated by letting the unlabeled cells stand for 30 min until they aggregated.

Live/Dead Cell Analysis. PC-3M cells were harvested with trypsin as described above and divided into three groups. The first group was labeled with EpCAM microbeads as described above and then sorted through the Prism Chip and collected at the outlets. The second group, the live control, was left unlabeled and was held on ice in FBS supplemented HBSS buffer during the sorting. The third group (dead control) was treated with a 70% methanol solution for 30 min to permeabilize the cell membrane. All cells were then stained with a live/dead viability kit (L3224, ThermoFisher) containing 10 μM EthD-1 and 1 μM Calcein AM for 45 min prior to analysis. Sample staining images are available in SI Figure S7.

WBC Depletion. Whole blood samples from healthy donors were collected in CellSave preservative tubes (CellSearch). The blood was

DOI: 10.1021/acsnano.8b07616
ACS Nano 2018, 12, 12692−12700

then diluted 1:1 with HBSS supplemented with 2% BSA and 5 mM EDTA. When spiked samples were evaluated, human prostate cancer cells were added to the diluted blood solution at an appropriate concentration. Dynabeads targeted to CD45 and CD15 (11153D, 11137D, ThermoFisher) were washed with buffer using a magnetic separator and then added to the blood/cell solution to achieve 10 and 2.5% concentrations by volume, respectively. The labeled blood was flowed through a simplified Prism Chip having two outlets and a single set of ferromagnetic separation guides, angled at 5°, and the effluent from the negative outlet was collected, stained using Syto 24 green fluorescent stain, and analyzed using the 10 outlet Prism Chip.

Processing of Hall Sensor Data. The Hall sensors are current biased using a DC source. The output signals were amplified and digitized on an Arduino Megas. Data were processed using a combination of custom-written and MATLAB-generated C code. The signals were filtered for high-frequency noise and then binned into sizes based on the areas under the signal and the signal peak values. Initial analog data were collected using a 4156A semiconductor parameter analyzer (Hewlett-Packard).

Orthotopic Xenograft Mouse Models for Prostate Cancer. All animal experiments were conducted according to the protocol approved by University of Toronto Animal Care Committee. A mouse xenograft model was prepared by orthotopic injection of human prostate cancer cell line, PC-3M. In each mouse, 1×10^6 cells were injected orthotopically into the right dorsolateral lobe of the prostate of 6−8 week old male athymic nude (nu/nu) mice. Mice were euthanized at designated time point after the injection (at 1, 2, 3, and 4 weeks, $n = 5$ mice per cohort for the first three time points, $n = 3$ mice per cohort for the final time point), and 500 μL of blood was collected by cardiac puncture for CTC analysis.

ASSOCIATED CONTENT

Supporting Information

The Supporting Information is available free of charge on the ACS Publications website at DOI: 10.1021/acsnano.8b07616.

Additional information on the fabrication of the microfluidic devices, chip design, and performance (PDF)

AUTHOR INFORMATION

Corresponding Author

*E-mail: shana.kelley@utoronto.ca.

ORCID

Edward H. Sargent: 0000-0003-0396-6495

Shana O. Kelley: 0000-0003-3360-5359

Author Contributions

⊥P.M.A. and M.M. contributed equally to this work.

Notes

The authors declare no competing financial interest.

ACKNOWLEDGMENTS

Research reported in this publication was supported by the Canadian Institutes of Health Research (Grant No. FDN-148415) and the National Cancer Institute of the National Institutes of Health (Grant No. R33CA204574). The content is solely the responsibility of the authors and does not necessarily represent the official views of the National Institutes of Health or the other funding agencies.

REFERENCES

(1) Massagué, J.; Obenauf, A. C. Metastatic Colonization by Circulating Tumour Cells. *Nature* **2016**, *529*, 298−306.

(2) Chaffer, C. L.; Weinberg, R. a. A Perspective on Cancer Cell Metastasis. *Science* **2011**, *331*, 1559−1564.

(3) Mohme, M.; Riethdorf, S.; Pantel, K. Circulating and Disseminated Tumour Cells-Mechanisms of Immune Surveillance and Escape. *Nat. Rev. Clin. Oncol.* **2017**, *14*, 155−167.

(4) Allard, W. J.; Matera, J.; Miller, M. C.; Repollet, M.; Connelly, M. C.; Rao, C.; Tibbe, A. G. J.; Uhr, J. W.; Terstappen, L. W. M. M. Tumor Cells Circulate in the Peripheral Blood of All Major Carcinomas but Not in Healthy Subjects or Patients with Non-malignant Diseases. *Clin. Cancer Res.* **2004**, *10*, 6897−6904.

(5) De Bono, J. S.; Scher, H. I.; Montgomery, R. B.; Parker, C.; Miller, M. C.; Tissing, H.; Doyle, G. V.; Terstappen, L. W. W. M.; Pienta, K. J.; Raghavan, D. Circulating Tumor Cells Predict Survival Benefit from Treatment in Metastatic Castration-Resistant Prostate Cancer. *Clin. Cancer Res.* **2008**, *14*, 6302−6309.

(6) Thiery, J. P. Epithelial-Mesenchymal Transitions in Tumour Progression. *Nat. Rev. Cancer* **2002**, *2*, 442−454.

(7) Aceto, N.; Bardia, A.; Miyamoto, D. T.; Donaldson, M. C.; Wittner, B. S.; Spencer, J. A.; Yu, M.; Pely, A.; Engstrom, A.; Zhu, H.; Brannigan, B. W.; Kapur, R.; Stott, S. L.; Shioda, T.; Ramaswamy, S.; Ting, D. T.; Lin, C. P.; Toner, M.; Haber, D. A.; et al. Circulating Tumor Cell Clusters Are Oligoclonal Precursors of Breast Cancer Metastasis. *Cell* **2014**, *158*, 1110−1122.

(8) Stott, S. L.; Hsu, C.-H.; Tsukrov, D. I.; Yu, M.; Miyamoto, D. T.; Waltman, B. a.; Rothenberg, S. M.; Shah, A. M.; Smas, M. E.; Korir, G. K.; Floyd, F. P.; Gilman, A. J.; Lord, J. B.; Winokur, D.; Springer, S.; Irimia, D.; Nagrath, S.; Sequist, L. V.; Lee, R. J.; et al. Isolation of Circulating Tumor Cells Using a Microvortex-Generating Herringbone-Chip. *Proc. Natl. Acad. Sci. U. S. A.* **2010**, *107*, 18392−18397.

(9) Poudineh, M.; Sargent, E. H.; Pantel, K. P.; Kelley, S. O. Profiling Circulating Tumour Cells and Other Biomarkers of Invasive Cancers. *Nat. Biomed. Eng.* **2018**, *2*, 72−84.

(10) Czechowska, K.; Johnson, D. R.; van der Meer, J. R. Use of Flow Cytometric Methods for Single-Cell Analysis in Environmental Microbiology. *Curr. Opin. Microbiol.* **2008**, *11*, 205−212.

(11) Riethdorf, S.; Fritsche, H.; Müller, V.; Rau, T.; Schindlbeck, C.; Rack, B.; Janni, W.; Coith, C.; Beck, K.; Jänicke, F.; Jackson, S.; Gornet, T.; Cristofanilli, M.; Pantel, K. Detection of Circulating Tumor Cells in Peripheral Blood of Patients with Metastatic Breast Cancer: A Validation Study of the CellSearch System. *Clin. Cancer Res.* **2007**, *13*, 920−928.

(12) Harouaka, R.; Kang, Z.; Zheng, S.-Y.; Cao, L. Circulating Tumor Cells: Advances in Isolation and Analysis, and Challenges for Clinical Applications. *Pharmacol. Ther.* **2014**, *141*, 209−221.

(13) Inglis, D. W.; Riehn, R.; Austin, R. H.; Sturm, J. C. Continuous Microfluidic Immunomagnetic Cell Separation. *Appl. Phys. Lett.* **2004**, *85*, 5093−5095.

(14) Pamme, N.; Wilhelm, C. Continuous Sorting of Magnetic Cells *via* On-Chip Free-Flow Magnetophoresis. *Lab Chip* **2006**, *6*, 974−980.

(15) Schneider, T.; Moore, L. R.; Jing, Y.; Haam, S.; Williams, P. S.; Fleischman, A. J.; Roy, S.; Chalmers, J. J.; Zborowski, M. Continuous Flow Magnetic Cell Fractionation Based on Antigen Expression Level. *J. Biochem. Biophys. Methods* **2006**, *68*, 1−21.

(16) Adams, J. D.; Kim, U.; Soh, H. T. Multitarget Magnetic Activated Cell Sorter. *Proc. Natl. Acad. Sci. U. S. A.* **2008**, *105*, 18165−18170.

(17) Poudineh, M.; Aldridge, P. M.; Ahmed, S.; Green, B. J.; Kermanshah, L.; Nguyen, V.; Tu, C.; Mohamadi, R. M.; Nam, R. K.; Hansen, A.; Sridhar, S. S.; Finelli, A.; Fleshner, N. E.; Joshua, A. M.; Sargent, E. H.; Kelley, S. O. Tracking the Dynamics of Circulating Tumor Cell Phenotypes Using Nanoparticle-Mediated Magnetic Ranking. *Nat. Nanotechnol.* **2017**, *12*, 274−282.

(18) Labib, M.; Mohamadi, R. M.; Poudineh, M.; Ahmed, S. U.; Ivanov, I.; Huang, C. L.; Moosavi, M.; Sargent, E. H.; Kelley, S. O. Single Cell mRNA Cytometry *via* Sequence-Specific Nanoparticle Clustering and Trapping. *Nat. Chem.* **2018**, *10*, 489−495.

(19) Tibbe, A. G. J.; de Grooth, B. G.; Greve, J.; Dolan, G. J.; Rao, C.; Terstappen, L. W. M. M. Magnetic Field Design for Selecting and Aligning Immunomagnetic Labeled Cells. *Cytometry* **2002**, *47*, 163−172.

DOI: 10.1021/acsnano.8b07616
ACS Nano 2018, 12, 12692−12700

(20) Goleman, K. P.; Sasada, I. High Sensitive Orthogonal Fluxgate Magnetometer Using Metglas Ribbon. *INTERMAG 2006 - IEEE Int. Magn. Conf.* **2006**, *42*, 522.
(21) Rao, C. C.; Chianese, D.; Doyle, G.; Miller, C.; Russell, T.; Sanders, R.; Terstappen, L. Expression of Epithelial Cell Adhesion Molecule in Carcinoma Cells Present in Blood and Primary and Metastatic Tumors. *Int. J. Oncol.* **2005**, *27*, 49−57.
(22) Ramsden, E. *Hall-Effect Sensors - Theory and Application*, 2nd ed.; Elsevier, 2006.
(23) Petruk, O.; Szewczyk, R.; Ciuk, T.; Strupiński, W.; Salach, J.; Nowicki, M.; Pasternak, I.; Winiarski, W.; Trzcinka, K. Sensitivity and Offset Voltage Testing in the Hall-Effect Sensors Made of Graphene. *Adv. Intell. Syst. Comput.* **2014**, *267*, 631−640.
(24) Pinto, A. M.; Gonçalves, I. C.; Magalhães, F. D. Graphene-Based Materials Biocompatibility: A Review. *Colloids Surf., B* **2013**, *111*, 188−202.
(25) Manzin, A.; Simonetto, E.; Amato, G.; Panchal, V.; Kazakova, O. Modeling of Graphene Hall Effect Sensors for Microbead Detection. *J. Appl. Phys.* **2015**, *117*, 17B732.
(26) Kumagai, Y.; Imai, Y.; Abe, M.; Sakamoto, S.; Handa, H.; Sandhu, A. Sensitivity Dependence of Hall Biosensor Arrays with the Position of Superparamagnetic Beads on Their Active Regions. *J. Appl. Phys.* **2008**, *103*, 07A309.
(27) Shevkoplyas, S. S.; Siegel, A. C.; Westervelt, R. M.; Prentiss, M. G.; Whitesides, G. M. The Force Acting on a Superparamagnetic Bead Due to an Applied Magnetic Field. *Lab Chip* **2007**, *7*, 1294−1302.
(28) Lowes, L. E.; Goodale, D.; Xia, Y.; Postenka, C.; Piaseczny, M. M.; Paczkowski, F.; Allan, A. L. Epithelial-to-Mesenchymal Transition Leads to Disease-Stage Differences in Circulating Tumor Cell Detection and Metastasis in Pre-Clinical Models of Prostate Cancer. *Oncotarget* **2016**, *7*, 12682.
(29) Ren, Y.; Huang, S. H.; Mosser, S.; Heuschkel, M. O.; Bertsch, A.; Fraering, P. C.; Chen, J. J. J.; Renaud, P. A Simple and Reliable PDMS and SU-8 Irreversible Bonding Method and Its Application on a Microfluidic-MEA Device for Neuroscience Research. *Micromachines* **2015**, *6*, 1923−1934.

DOI: 10.1021/acsnano.8b07616
ACS Nano 2018, 12, 12692−12700